



Contents lists available at ScienceDirect

Arabian Journal of Chemistry

journal homepage: www.ksu.edu.sa

Preparation of chlorophyll compounds and simulation of DFT optical properties assisted screening of photosensitizers from *Ginkgo biloba* leaves

Hong Shen^{a,b}, Changwei Zhang^a, Hao zhou^{a,*}, Chuan Li^a, Hua Yuan^a, Jianxin Jiang^b, Chengzhang Wang^{a,*}

^a Chemical Engineering of Forest Products, Institute of Chemical Industry of Forest Products, Chinese Academy of Forestry, Nanjing 210042, China

^b Department of Chemistry and Chemical Engineering, Beijing Forestry University, Beijing 100083, China

ARTICLE INFO

Keywords:

Chlorophyll
Ginkgo biloba
 Photosensitizers
 DFT
 TD-DFT

ABSTRACT

Chlorophyll compounds (Chls) from *Ginkgo biloba* leaves (GBL) are non-toxic natural pigments characterized by highly conjugated molecules and special spectra, making them ideally potential photosensitizers (PSs) in photodynamic therapy (PDT). In this study, 4 Chls were isolated from *Ginkgo biloba* polyphenols (GBPPs) wastes by using silica gel column separation and high performance liquid chromatography (HPLC). In addition, two new chlorophyll derivatives were successfully synthesized with chlorin e6 as the primary raw material. To evaluate and identify superior chlorophyll PSs, Density Functional Theory (DFT) and Density Functional Theory (TD-DFT) were employed to decode the microscopic and spectral properties of *Ginkgo biloba* Chls (GBChls). The spectral absorption, optical stability and reactive oxygen species (ROS) production of GBChls were further analyzed through comparisons of their frontier molecular orbital layout, charge distribution and excitation energy properties. Our results show that about 63 % absorption in the Q band for 14 GBChls comes from the $\pi \rightarrow \pi^*$ transition from the highest occupied orbital (HOMO) to the lowest unoccupied orbital (LUMO), indicating the favorable delocalization effect of these GBChls. In particular, those GBChls with the long chain of the phytol group exhibited higher total electron energy and thus could significantly increase the light stability. However, the large spatial volume and hydrophobicity of these compounds with the phytol group chain was unfavorable for cellular uptake, leading to low ROS in cells. The electronegativity of porphyrin macrocycles in GBChls positively correlates with the intracellular ROS production rate, meaning that the former likely promotes the energy transfer between PSs and molecular oxygen during type II photoreaction. Among the GBChls, chlorin e6 demonstrated the highest ROS yields in DMF, while purpurin 18 compounds displayed long-wavelength absorption (698 nm), strong Q-band absorption, good optical stability, and high intracellular ROS production. Our findings highlight that chlorin e6 and purpurin 18 are most potential PSs anticancer drugs and offer new research perspectives for the processing and utilization of GBL resources.

1. Introduction

Ginkgo biloba (GB) is the oldest relict plant endemic to China and is known as a “living fossil”, and *Ginkgo biloba* leaf (GBL) contains various natural active substances such as flavonoids, lactones, and lipids (Li et al., 2023, Liu et al., 2022). Polyphenols (PPs) and chlorophyll compounds (Chls) are fat-soluble lipid compounds in GBL, and they have the efficacy of preventing hypertension, anti-tumor, protecting liver and treating senile dementia (Yang et al., 2011, Boateng et al., 2023). In particular, Chls, a class of organic compounds containing asymmetric

conjugated porphine macrocycles, play an essential role in coloration and photodynamic therapy (PDT) (Wang and Grimm., 2021, Warszyńska et al., 2023). Researchers have developed various photosensitizers (PSs) for PDT, including Chls, among which chlorin e6 has been clinically applied (Lu et al., 2022, Liao et al., 2023). Although large amounts of Chls-rich wastes are produced during extracting GB polyphenols (GBPPs), how to efficiently separate Chls from the wastes is still being investigated.

GB chlorophylls, composed of chlorophyll *a* and *b*, can be converted into various chlorophyll derivatives under the influence of light, oxygen,

Peer review under responsibility of King Saud University.

* Corresponding authors.

E-mail addresses: zhouhaolhs@163.com (H. Zhou), wangczlhs@sina.com (C. Wang).

<https://doi.org/10.1016/j.arabjc.2023.105549>

Received 19 October 2023; Accepted 10 December 2023

Available online 15 December 2023

1878-5352/© 2023 The Author(s). Published by Elsevier B.V. on behalf of King Saud University. This is an open access article under the CC BY-NC-ND license (<http://creativecommons.org/licenses/by-nc-nd/4.0/>).

heat, enzymes, acids and bases (Chen et al., 2023, Pérez-Gálvez et al., 2023). They possess asymmetric chemical structures and multi-substituted active functional groups, making them meet the basic PSs requirements as high-efficiency PDT anti-cancer drugs (Qiu et al., 2023, Zhou et al., 2023). It has been shown that the degree of electron delocalization affects the chemical and photophysical properties of PSs (Lan et al., 2019, Zheng et al., 2023). The basic carbon frame of the GBChls belongs to the aromatic azalene ring structure, in which the multi-electron carbon-carbon double bond and the electron-poor carbon-oxygen double bond can conjugate with the porphin group and constitute the largest range of π -electron system (Cai et al., 2021, Pucci et al., 2021). The large conjugated porphin structure of GBChls thus gives them strong absorption capacity in the near-infrared region, which can effectively enhance the tissue penetration ability and reactive oxygen species (ROS) yield of PSs. Quantitative structure-activity relationship studies have shown that the anticancer efficacy of Chls are closely related to their structures, including three-dimensional space, connection position, electrostatic matching, water-lipid solubility, and redox potential (Chin et al., 2023, Warszyńska et al., 2023). In this scenario, introducing active functional groups on the porphin ring is the critical and preliminary step for developing new PDT drugs. In particular, the introduction of active functional groups on the porphin ring and the structural modification of the outer ring are important preliminary work for ideal PDT drugs (Szafraniec et al., 2023, Brandis et al., 2006). Many GBChls contain β -ketone ester, α -ketone ester, aromatic and fatty carboxylic ester structures in the C-D ring end. These electron-absorbing polyoxy groups combined with the hydrocarbon groups in the A-B ring give good water-lipid solubility to the macrocyclic molecules of porphin, which ensures the bioavailability necessary for the PDT process (Zahra et al., 2023, Warszyńska et al., 2023). Simultaneously, introducing oxygen-containing substituents (e.g., aldehyde groups, ketone groups and hydroxyl groups) into the chlorophylls can greatly improve the optical properties of macrocyclic molecules (Wahnou et al., 2023, Singh et al., 2023). Thus, separating GBChls from GBPPs saponified

wastes is of paramount significance for investigating their application in PDT, which can improve the comprehensive utilization rate of GBL active substances and select new PSs with excellent properties for clinical applications in PDT.

Currently, researchers mainly screen and evaluate PSs from the macroscopic level, such as light stability, optical properties, ROS yield, cell experiments and animal experiments (Arnaut et al., 2023, Bartusik-Aebisher et al., 2023). However, these experiments are expensive and time-consuming, and there is limited research on the microscopic mechanism of PS. Density Functional Theory (DFT) and Time-dependent Density Functional Theory (TD-DFT) programs are important tools for investigating PSs and their microstructure change mechanisms, and the methods are also time-saving and cost-effective (Sammüller et al., 2023, Zhang et al., 2023). For example, Sen S used DFT to identify local excited states or charge transfer states, and emphasized the importance of charge transfer effect in changing the absorption intensity of chlorophyll dimers (Liu et al., 2021). In addition, Jiang D employed DFT to establish zigzag edge and armchair edge cluster models with oxygen-containing groups, to investigate the adsorption of CO₂ by biomass pyrolysis char (Jiang et al., 2023). DFT and TD-DFT simulation can decipher the interaction mechanism of various substances in the research system at the molecular level, and can well predict the structure-property relationship and the internal mechanism of the research system (Rocha et al., 2023, Wang et al., 2023, Leal et al., 2023).

In this study, the GBChls were isolated and purified from the GBL and waste of GBPPs. Then, DFT was used to simulate the microscopic and spectral properties of Chls, and their unique structure and excellent spectral characteristics were revealed from the microscopic perspective, which can help us to further understand the relationship between their structure and properties. Finally, according to the compounds' optical properties and ROS yields, the PSs with superior performance were selected. The specific research idea is shown in Fig. 1.

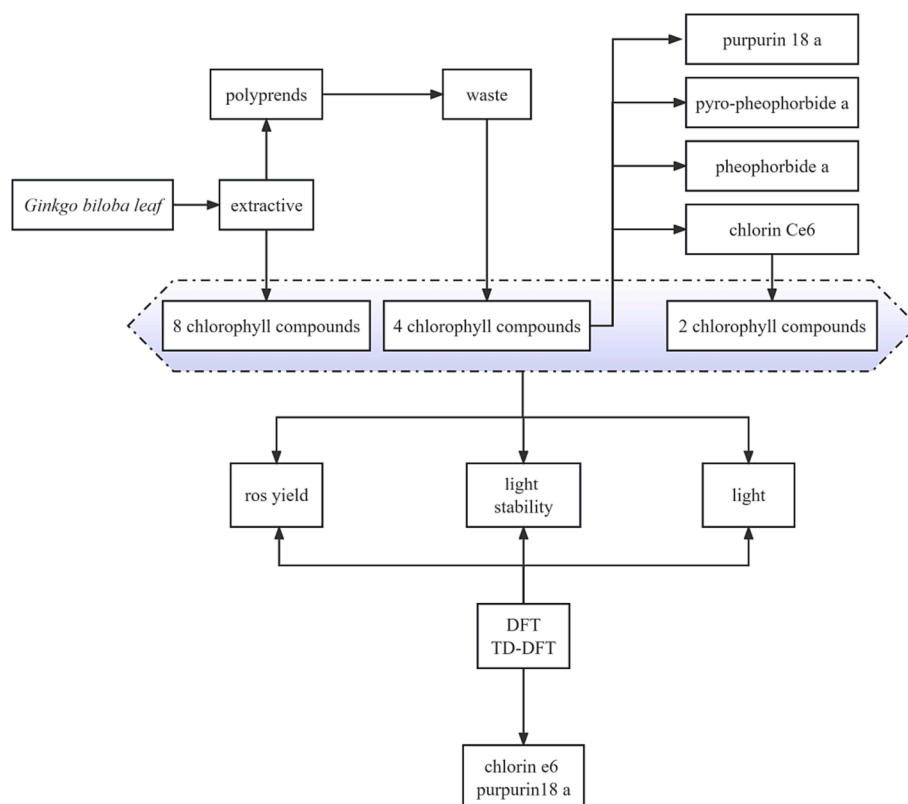


Fig. 1. Schematic illustration of Chls PSs preparation and study.

2. Materials and methods

2.1. Materials

Methanol, ethanol, iodomethane, anhydrous sodium sulfate were purchased from Sigma-Aldrich (Shanghai, China). Dichloromethane (DCM), ethyl acetate, ethyl ether and acetone were obtained from Shanghai Yien Chemical Technology Co., Ltd. (Shanghai, China). Anhydrous potassium carbonate, N,N-Dimethylformamide (DMF) were purchased from Aladdin Biochemical Technology Co., Ltd. (Shanghai, China). Sodium bicarbonate and toluene were provided by Ponsure Biological Technology Co., Ltd. (Shanghai, China). Sodium bisulfate, sodium chloride and magnesium sulfate were purchased from Sinopharm Chemical Reagent Co., Ltd. (Shanghai, China).

2.2. Preparation of GBCChls

2.2.1. Extract of GBL fat-soluble pigments

The GBL was pulverized and sieved through an 80-mesh sieve. The extraction conditions were as follows: solid-to-liquid ratio of 1:5 (g/mL), 3 extraction cycles, extraction temperature of 45°C, and extraction time of 2 h. After extraction, the extract was combined, filtered, and concentrated under reduced pressure to obtain a concentrated extract. Then concentrated extract was dissolved in acetone and mixed with an equal amount of ether by gentle shaking for 2 min. The solution was subsequently supplemented with an equal volume of water, facilitating the separation into two distinct layers. The upper layer comprised of fat-soluble pigments soluble in ether, while the lower layer encompassed water-soluble impurities and was discarded. Finally, the same volume of water was added, and the residual impurities were removed by repeated extraction for three times. The ether layer was collected and vacuum concentrated to obtain refined ointment A. The above extraction process was conducted under light-protected conditions.

2.2.2. Separation of GBCChls

The ointment A was dissolved in a small amount of DCM, and a silica gel column was used for gradient elution with a petroleum ether-ethyl acetate system. Components with similar polarity were combined through thin-layer chromatography (TLC). Subsequently, these components underwent further separation and purification via high-performance liquid chromatography (HPLC) to obtain the corresponding 8 Chls (compounds 4, 6, 7, 8, 10, 11, 12 and 14) (Shen et al., 2023).

Ointment A was added with about 10 % sodium hydroxide-ethanol solution (water: ethanol = 7: 1) according to the solid-liquid ratio of 1: 10, the stirring speed was 260 r/min, the temperature was 70 °C, and the saponification reaction was 3 h. The saponification solution was extracted with hexane and then separated and purified to obtain the finished polyvalent alcohol. The remaining saponification solution was adjusted to neutral with HCl, and the uplifted lipid-soluble compounds were taken and dried in a vacuum drying oven.

The crude separation and purification were carried out via silica gel column packed with 200–300 mesh silica gel. A gradient elution was performed using an eluent of petroleum ether and ethyl acetate (1 %–100 % ethyl acetate). The similar fractions were determined by TLC, then concentrated under reduced pressure to obtain Fr.1–Fr.6, in which Fr.1–Fr.3 were compounds with red fluorescence, Fr.4 was brown oily compound, and Fr.5–6 were orange paste. The Fr.1 and Fr.2 were purified by gradient elution with petroleum ether and ethyl acetate (1 %–20 % ethyl acetate) to obtain the mixture of compounds 5, 9 and 13. The mixture was further purified by HPLC to isolate the monomers of compounds 5, 9 and 13 respectively with methanol/ethyl acetate 4:1 vol ratios mobile phase. The Fr.3 components were purified by gradient elution using DCM (1 %–5% methanol) system (0.2 % formic acid was added to the elution system) to obtain compound 1. The components of Fr.4 were distilled under reduced pressure at a vacuum of 35–45 Pa and a temperature of 145–180 °C, and the distillate was collected to obtain

compound 15. The above separation process is conducted under light-protected conditions.

2.2.3. Methylation of chlorin e6

2.2.3.1. Preparation of chlorin e6 trimethyl ester. 1.00 g (1.68 mmol) compound 1 was dissolved in 20 mL DMF, and then 4.60 g (33.28 mmol) anhydrous potassium carbonate and 2.28 g (16.06 mmol) iodomethane were added. The reaction was stirred at room temperature for 2 h under nitrogen protection and light protection. After the reaction, it was diluted with 100 mL DCM and transferred to a 250 mL separation funnel. It was washed with water for 5 times, 100 mL each time, and then washed once with 100 mL brine. The organic layer was collected, and dried with anhydrous sodium sulfate, and filtered to obtain the crude product. The crude product was separated and purified by 200–300 mesh silica gel column chromatography, with DCM: ethyl acetate (97:3) as the eluent. Finally, a black powder of 0.91 g (compound 2, 1.43 mmol) was obtained with a yield of 85 %. The above purification process was also carried out under light protection conditions.

2.2.3.2. Preparation of chlorin e6 dimethyl ester. 541 mg (0.91 mmol) chlorin e6 was dissolved in 50 mL 5 % H₂SO₄ methanol solution and stirred for 10 h at room temperature in the dark under nitrogen protection. After completion of the reaction, the methanol solvent was evaporated. The residue was then diluted with DCM and washed thoroughly with 100 mL deionized water, saturated sodium bicarbonate and brine, respectively. The organic layer was separated, dried over anhydrous sodium sulfate, and concentrated to obtain crude product. The crude product was further purified using silica gel column chromatography with a mobile phase consisting of DCM/methanol = 15:1. Finally, 505 mg (compound 3 0.81 mmol) of the desired product was obtained with a yield of 89 %. All the purification process was also carried out under light protection conditions.

2.3. Structure optimization and spectral simulation of GBCChls

The ground state geometry structure of 14 Chls was optimized using the DFT method with the B3LYP functional and 6-31G (d) basis set. The total electron energy, the frontier molecular orbital energy, and the electron cloud density distribution of Chls were calculated. Based on the optimized geometry structure of the ground state, the excitation energy and absorption spectra of the above 14 Chls were calculated and simulated by TD-DFT. All the above calculations were performed by Gaussian 09 program.

2.4. Testing for light stability

Chls were dissolved in ethanol at a concentration of 5 μM and placed in a 1 × 1 cuvette, respectively. The sample solutions were irradiated with 660 nm LED light at a light intensity of 1.5 mW/cm². The absorption spectra of the samples were recorded at 0, 2, 15, 25, 45, and 60 min using a UV-vis absorption spectrometer V-550. The relative values of the absorption intensity of the Q band I_t/I₀ were plotted against the time of illumination to respond to the percentage of drug residues. I_t and I₀ represent the absorption intensity of 660 nm at t and initial time, respectively.

2.5. In vitro ROS assay for Chls

2.5.1. ROS generation of Chls in DMF by DPBF

A mixture of the test drug and DMF of DPBF was prepared at final concentrations of 5 and 50 μM, respectively, and then placed in a 1 × 1 cm cuvette. The absorbance of the test solution at 417 nm was measured at 10 s intervals for 2 min using 660 nm LED light with an intensity of 1.5 mW/cm². The reaction rate constant K_{obs} was calculated according

to Equation (1).

$$\ln\left(\frac{A_0}{A_t}\right) = k_{obs} \times t \quad (1)$$

A_0 and A_t represented the absorbance of the solution at time 0 s and t , respectively.

Afterwards, the single linear state oxygen yields were calculated by comparing the rate constants of the samples with those of the reference methylene blue according to Equation (2).

$$\frac{k(PS)}{k(ref)} = \frac{\varnothing(PS)}{\varnothing(ref)} \quad (2)$$

2.5.2. ROS generation of Chls in vitro

The cells were prepared into a cell suspension with a concentration of 5×10^4 cells/mL. 200 μ L cell suspension (1×10^4 cells per well) was

added to each well in the 24 well cell culture plate. The 24 well cell culture plate was placed in a 37 °C, 5 % CO₂ incubator for 24 h, and the corresponding drug-containing medium was added according to the group settings, and a negative control group was established. After 24 h of drug action, the fresh medium containing DCFH-DA 10 μ M was replaced and stained for 30 min. PBS was washed three times after irradiation (660 nm, 1.5 mW/cm²) for 10 min. Dapi was diluted at a ratio of 1:1000 and added to a 24 well plate. After incubation in the dark for 20 min, PBS was washed three times. 1 mL PBS was added, and the expression was observed under a confocal microscope.

Table 1
Structures and numbers of 14 GBChls.

| No. | Compounds name | Ring (E) | R | R ₂ | R ₅ | R ₆ |
|-----|-----------------------------------|----------|-----------------|-----------------|------------------------------------|--------------------|
| 1 | Chlorin compounds | | R ₁ | | | |
| 1 | Chlorin e6 | E1 | H | CH ₃ | CH ₂ COOH | COOH |
| 2 | Chlorin e6 trimethyl ester | E1 | CH ₃ | CH ₃ | CH ₂ COOCH ₃ | COOCH ₃ |
| 3 | Chlorin e6 dimethyl ester | E1 | CH ₃ | CH ₃ | CH ₂ COOCH ₃ | COOH |
| 4 | Chlorophyll a compounds | | R ₁ | R ₂ | R ₃ | R ₄ |
| 4 | Pheophytin a | E2 | Phytyl | CH ₃ | COOCH ₃ | H |
| 5 | Pheophorbide a | E2 | H | CH ₃ | COOCH ₃ | H |
| 6 | 13 ² -OH-pheophytin a | E2 | Phytyl | CH ₃ | COOCH ₃ | OH |
| 7 | 13 ² -OH-pheophytin a' | E2 | Phytyl | CH ₃ | OH | COOCH ₃ |
| 8 | Pyro-pheophytin a | E2 | Phytyl | CH ₃ | H | H |
| 9 | Pyro-pheophorbide a | E2 | H | CH ₃ | H | H |
| 10 | Chlorophyll b compounds | | R ₁ | R ₂ | R ₃ | R ₄ |
| 10 | Pheophytin b | E2 | Phytyl | CHO | COOCH ₃ | H |
| 11 | 13 ² -OH-pheophytin b | E2 | Phytyl | CHO | COOCH ₃ | |
| 12 | 13 ² -OH-pheophytin b' | E3 | Phytyl | CHO | OH | COOCH ₃ |
| 13 | Purpurin18 compounds | | R ₁ | R ₂ | | |
| 13 | Purpurin18 a | E3 | H | CH ₃ | | |
| 14 | Phy-purpurin18 a | E3 | Phytyl | CH ₃ | | |

3. Results and discussion

3.1. Structural identification of the compounds

In this study, four Chls and one phytol were isolated from the saponification liquid waste during the processing of GBPPs. The four Chls separated from the GBPPs saponification solution are pheophorbide a, pyro-pheophorbide a, purpurin 18, and chlorin e6, respectively. Furthermore, two chlorophyll-based photosensitizers were synthesized *via* esterification reaction using chlorin e6 as a raw material. The structures of seven compounds, i.e., pheophorbide a (compound 5), pyro-pheophorbide a (compound 9), purpurin 18 (compound 13), chlorin e6 (compound 1), phytol (compound 15), chlorin trimethyl ester (compound 2), and chlorin dimethyl ester (compound 3), were confirmed by ^1H NMR, IR, and MS analysis (Fig. S1-21) (Duan et al., 2002, Hu et al; 2010, Hooper, et al.,). Furthermore, in past studies, we also isolated eight Chls from GBL by silica gel column separation and HPLC. The structure and number of 14 kinds of GBChls are depicted in Table 1.

3.2. Effect of GBPPs saponification solution on the structure of GBChls

Chlorophyll mainly exists in the fresh GBL. The isolated and purified Chls from GBL and the GBPPs saponification solution primarily consist of pheophytin and pheophorbide compounds. Due to the instability of chlorophyll, various factors such as light, oxygen, acid, alkali, and enzymes can facilitate the conversion of chlorophyll into chlorophyll derivatives (Wang et al., 2023, Hu et al., 2021). The transformation process is depicted in Fig. 2. During the processing, heating Chls triggered demagnesiation and demethylation reactions, converting them into pheophytin and pyro-pheophytin (Kang et al., 2018, Chen et al., 2018). Furthermore, the exposure of GBL and GBE to air during processing facilitated the oxidation of chlorophyll and pheophytin, thus generating of chlorophyll oxide derivatives such as 13²-OH pheophytin

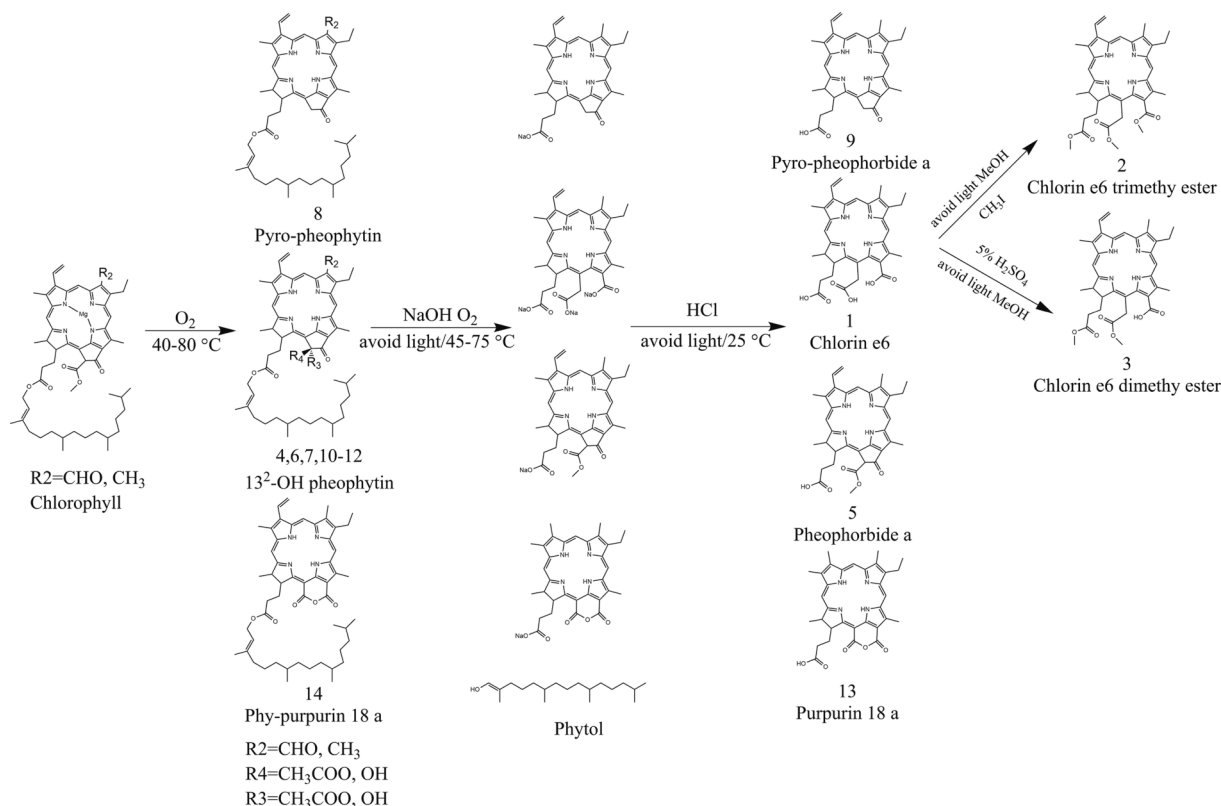


Fig. 2. The transformation route of chlorophyll in GBL during processing.

and purpurin (Chen et al., 2018). The GBE was saponified, resulting in the separation of phytol from Chls (Pérez-Gálvez et al., 2023). The saponification solution was then neutralized with HCl, converting Chls into various pheophorbide such as pyro-pheophorbide a, pheophorbide a, purpurin 18 a, and chlorin e6 (Fig. 2).

3.3. Geometric structure optimization of Chls molecules

The total electron energy of 14 Chls were calculated by DFT/B3LYP/6-31G (d). As shown in Fig. 3, chlorophyll *b* compounds (compounds

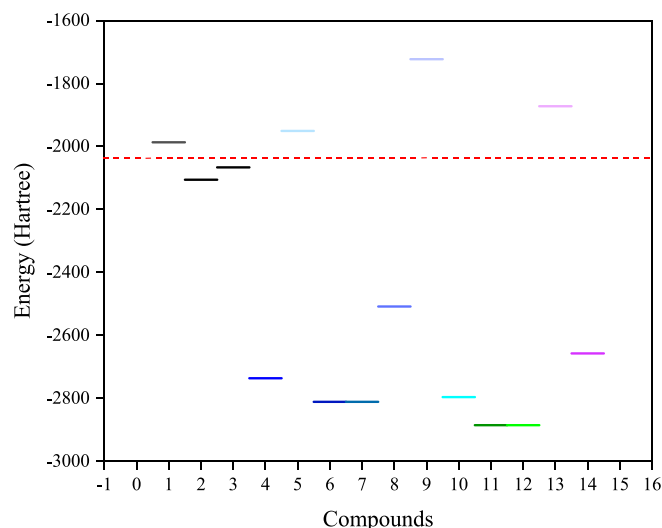


Fig. 3. Total electron energy diagram of 14 Chls. (The chlorophyll compounds above the red dotted line are not esterified by phytol and methyl, while those below the red dotted line are esterified by phytol and methyl.).

10–12) have total electron energy values ranging from -2885.13 to -2809.92 Hartree that are generally lower than those of other Chls, indicating more stable structures of chlorophyll *b* compounds. In addition, the chlorophyll *a* compounds (compounds 4, 6, 7 and 8) and purpurin 18 a compound (compound 14) with the phytol group long chains are all located below the red dotted line. On the other hand, Chls (compounds 5, 9 and 13) without phytol group are all positioned above the red dotted line. This indicates that the presence of phytol group can significantly reduce the energy of Chls. Notably, the esterification of chlorin compounds (compounds 2 and 3) can also decrease their total electron energy. This means that esterified Chls can enhance the stability of the PSs, and the longer the esterified alkyl chain is, the greater the energy reduction will be, resulting in a more stable compound.

The DFT optimization results reveal that the conjugated aromatic rings of the 14 Chls are predominantly planar, as depicted in Fig. S22. However, the external groups of Chls can induce some extent of distortion in their conjugated aromatic rings. The photoactive distorted configurations can enhance spin-orbit coupling and improve intersystem crossing (ISC) efficiency (Udrea et al., 2023). Therefore, the existence of twisted configurations in Chls may play a crucial role in promoting efficient energy and electron transfer processes that are essential for both biological and photochemical reactions.

The methyl esterified chlorin compounds' (compounds 2 and 3) porphyrin macrocyclic dihedral angle ($\angle C_{20}C_{10}C_5C_{15}$) decreased by $8.23 \sim 8.33$ (Table 2). This suggests that the methyl esterification of chlorin e6 can promote the distortion of conjugated aromatic rings of porphyrins. Furthermore, the conjugated aromatic ring distortion degree of phy-purpurin 18 a (compound 14, $\angle C_{20}C_{10}C_5C_{15}$, -168.03) and pyro-pheophytin a (compound 8, $\angle C_{20}C_{10}C_5C_{15}$, 173.58), both with the long chain of phytol, were larger than those of purpurin 18 a (compound 13, $\angle C_{20}C_{10}C_5C_{15}$, 176.18) and pyro-pheophorbide a (compound 9, $\angle C_{20}C_{10}C_5C_{15}$, 177.04) without phytol. According to Fig. S22, the long phytol chain of phy-purpurin 18 a (compound 14) and pyro-pheophytin a (compound 8) is folded together with the porphyrin macrocycle, which exerts a greater influence on the porphyrin macrocycle and results in a higher degree of distortion in the conjugated aromatic ring. As shown in Table 2, the conjugated aromatic ring distortion of porphyrins in chlorophyll *a* and *b* compounds (compounds 4–12) with a five-membered ring structure are significantly lower compared to that of purpurin 18 compounds (compounds 13 and 14) and chlorin compounds (compounds 1–3). This suggests that the structure of Chls containing a five-membered ring is more stable, resulting in a less impact of substituents around the porphyrin macrocycle on its distortion.

In the porphyrin ring of Chls, $\angle C_6N_{22}C_9$ is the smallest among the four $\angle CNC$ angles (Table 2). When the R_2 group of the B ring is an aldehyde group (compounds 10–12), the $\angle C_6N_{22}C_9$ angle falls within a range of 106.22 to 106.26 degrees. On the other hand, when the R_2 group is a methyl group (compounds 4–9), the $\angle C_6N_{22}C_9$ angle ranges from 105.03 to 105.65 degrees. These observations indicate that the presence of an

aldehyde group on the B ring increases the $\angle C_6N_{22}C_9$ angle. In the A ring with the same substituent, the corresponding $\angle C_1N_{21}C_4$ angle remains relatively constant. When E is a five-membered ring (compounds 4–12), the $\angle C_{11}N_{23}C_{14}$ angle is between 109.47 and 109.67 . When E is a six-membered ring (compounds 13 and 14), the $\angle C_{11}N_{23}C_{14}$ angle ranges from 110.41 to 110.46 degrees. Additionally, when R_4 and R_5 do not form a ring (compounds 1–3), the $\angle C_{11}N_{23}C_{14}$ angle is 111.82 and 111.96 degrees. These results indicate that the smaller the E ring, the stronger the binding to the C ring, resulting in a smaller angle of $\angle C_{11}N_{23}C_{14}$.

3.4. Molecular orbital analysis of Chls

To better understand the molecular electronic structure of Chls, we used DFT-B3LYP/6-31G (d) basis set to simulate molecular orbital of 14 Chls. As shown in Fig. S23-1, and Fig. S23-2, the the highest occupied molecular orbital (HOMO) and the lowest unoccupied molecular orbital (LUMO) represent delocalized π orbital and π^* orbital, respectively. These orbitals are primarily influenced by the four pyrrole rings and the methylene groups attached. The energy gap (Eg) value is closely related to the chemical reactivity, kinetic stability, and optical properties of molecules in the frontier molecular orbital (FMO) region (Choudhury et al., 2023; Diers et al., 2021). The smaller the Eg means the greater the molecular polarizability and chemical reactivity but poorer kinetic stability (Bourne-Worster et al., 2023; Reiter et al., 2022).

Theoretically, the properties of substituents can influence the size of the HOMO, LUMO, and Eg. Introducing a substituent with strong electron-withdrawing ability will reduce the HOMO (Zhang et al., 2017; Kang et al., 2023). However, it will simultaneously reduce LUMO and Eg if a longer conjugated group is introduced (Duan et al., 2023). Narrowing the energy gap of Eg will increase the electron transfer efficiency, facilitating the formation of free radical anions and cations (Zhang et al., 2017). This ultimately leads to higher photochemical activity of Chls as photosensitizers. As shown in Fig. 4, compared with the compounds (compounds 1–9, 13, 14) with electron-donating methyl group at C7, those with electron-withdrawing aldehyde group (compounds 10–12) have lower HOMO, HOMO-1, LUMO and LUMO + 1, and higher Eg (compounds 1–9: 2.45072 – 2.50512 , compounds 13 and 14: 2.29296 – 2.30384 , compounds 10–12: 2.570944 – 2.579648). Furthermore, compared with chlorin compounds (compounds 1–3) and chlorophyll *a* compounds (compounds 4–9), the purpurin 18 compounds (compounds 13 and 14) have lower HOMO, HOMO-1, LUMO, LUMO + 1 and Eg (compounds 1–3: 2.47792 – 2.50512 , compounds 4–9: 2.45072 – 2.47248 , compounds 13 and 14: 2.29296 – 2.30384). It can be attribute to the six ring of purpurin 18 prolongs the conjugation of porphine macrocycles. Therefore, purpurin 18 has good chemical reactivity, large polarizability and low kinetic stability relative to other Chls.

Table 2

The structural data of 14 GBChls after DFT-B3LYP/6-31G (d) optimization: dihedral angle $\angle C_{20}C_5C_{15}C_{10}$ and $\angle CNC$ ($\angle C_6N_{22}C_9$, $\angle C_{11}N_{23}C_{14}$, $\angle C_{16}N_{24}C_{19}$, $\angle C_1N_{21}C_4$).

| Compounds | $\angle C_{20}C_5C_{15}C_{10}$ | $\angle C_6N_{22}C_9$ | $\angle C_{11}N_{23}C_{14}$ | $\angle C_{16}N_{24}C_{19}$ | $\angle C_1N_{21}C_4$ |
|-----------|--------------------------------|-----------------------|-----------------------------|-----------------------------|-----------------------|
| 1 | 172.99 | 105.16 | 111.82 | 108.38 | 110.77 |
| 2 | 164.76 | 105.21 | 111.88 | 108.34 | 110.81 |
| 3 | 164.66 | 105.20 | 111.96 | 108.33 | 110.81 |
| 4 | 173.45 | 105.58 | 109.59 | 109.28 | 110.89 |
| 5 | 174.91 | 105.63 | 109.48 | 108.6 | 110.92 |
| 6 | 174.83 | 105.22 | 109.67 | 109.26 | 110.88 |
| 7 | 174.48 | 105.52 | 109.67 | 109.14 | 110.88 |
| 8 | 173.58 | 105.65 | 109.51 | 108.96 | 110.93 |
| 9 | 177.04 | 105.65 | 109.47 | 108.97 | 110.94 |
| 10 | 174.17 | 106.26 | 109.52 | 109.17 | 110.85 |
| 11 | 175.06 | 106.24 | 109.62 | 109.16 | 110.38 |
| 12 | 174.02 | 106.22 | 109.61 | 108.69 | 110.85 |
| 13 | -168.03 | 105.05 | 110.46 | 108.52 | 110.71 |
| 14 | 176.18 | 105.03 | 110.41 | 108.45 | 110.67 |

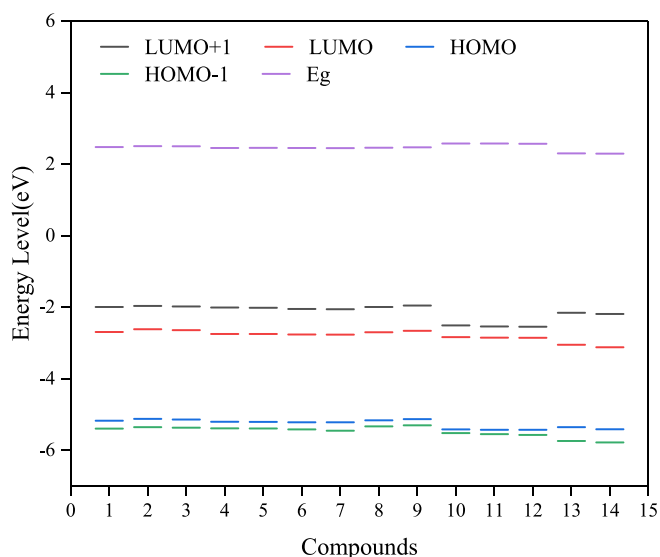


Fig. 4. Simulated HOMO, HOMO-1, LUMO, and LUMO + 1 orbitals as well as the Eg.

3.5. Optical studies of Chls

We initially employed an ultraviolet spectrophotometer and a fluorescence spectrophotometer to measure the absorption spectra and fluorescence spectra of the 14 Chls dissolved in a methanol solvent (Fig. S25). Subsequently, the electronic absorption spectra (Fig. S25) of the 14 Chls were studied by TD-DFT/B3LYP/6-31G(d) method, which provided theoretical constraints for our experimental results. Meanwhile, to better understand the electronic transition properties associated with different absorption bands, we compared the primary excited state energy (eV), excitation wavelength, orbital composition, and oscillator strength (f) corresponding to each absorption band (Table 3). This analysis allows us to examine the specific characteristics and properties of the electronic transitions occurring within the Chls.

The 14 Chls exhibit similar absorption characteristics (Fig. S25), with strong absorption peaks (Soret absorption band) at about 355–386 nm and moderate intensity Q absorption bands at 575 nm–600 nm. Compared to the experimented values, the calculated absorption characteristic peaks of 14 Chls show a blue shift of 38.69–56.06 nm for the S band and a blue shift of 60.59–81.49 nm for the Q band (Fig. S25 and Fig. 5). Although the absolute values differ from the experimental results, the trend of the ultraviolet spectral absorption of the Chls remains

Table 3

The calculated UV–vis parameters of 14 Chls: maximum wavelength (λ_{\max}), excitation energy (Ee), oscillator strength (f), and major contributions of all studied systems.

| Compounds | Ee/eV | f | Main configurations | λ_{\max}/nm |
|-----------|--------|--------|---|----------------------------|
| 1 | 2.0659 | 0.2242 | H-1 \rightarrow L 0.10093 H-1 \rightarrow L + 1 0.29417 H \rightarrow L 0.62896 | 600.14 |
| 2 | 2.0650 | 0.2177 | H-1 \rightarrow L + 1—0.30102 H \rightarrow L 0.63297 | 600.41 |
| 3 | 2.0694 | 0.2139 | H-1 \rightarrow L + 1 0.29961 H \rightarrow L 0.63263 | 599.14 |
| 4 | 2.0878 | 0.2524 | H-1 \rightarrow L + 1—0.28832 H \rightarrow L 0.63913 | 593.84 |
| 5 | 2.0754 | 0.2561 | H-1 \rightarrow L + 1—0.28999 H \rightarrow L 0.63886 | 597.39 |
| 6 | 2.0812 | 0.2553 | H-1 \rightarrow L + 1—0.28998 H \rightarrow L 0.63920 | 595.74 |
| 7 | 2.0658 | 0.2636 | H-1 \rightarrow L + 1—0.28906 H \rightarrow L 0.64029 | 600.17 |
| 8 | 2.0654 | 0.2357 | H-1 \rightarrow L + 1—0.29304 H \rightarrow L 0.63656 | 600.30 |
| 9 | 2.0753 | 0.2456 | H-1 \rightarrow L + 1—0.29766 H \rightarrow L 0.63545 | 597.44 |
| 10 | 2.1656 | 0.1381 | H-1 \rightarrow L + 1 0.34912 H \rightarrow L 0.60021 | 572.51 |
| 11 | 2.1591 | 0.1490 | H-1 \rightarrow L + 1 0.35041 H \rightarrow L 0.60098 | 574.24 |
| 12 | 2.1489 | 0.1458 | H-1 \rightarrow L + 1 0.34761 H \rightarrow L 0.60181 | 576.98 |
| 13 | 1.994 | 0.3032 | H-1 \rightarrow L + 1 0.23933 H \rightarrow L 0.65371 | 621.71 |
| 14 | 1.9897 | 0.2825 | H-1 \rightarrow L 0.10534 H-1 \rightarrow L + 1 0.22948 H \rightarrow L 0.65417 | 623.12 |

consistent. Upon analyzing the orbital contributions to the molecular excitation energies of the 14 compounds, we found that approximately 63 % of the Q band of Chls arise from $\pi \rightarrow \pi^*$ transitions between the HOMO and the LUMO. Additionally, about 30 % of the transitions originate from HOMO-1 to LUMO + 1. This indicates that Chls exhibit good delocalization effects within their molecular structures.

The maximum absorption wavelength of chlorin compounds in the S band experiment is 400 nm, and the maximum value in the Q band region is 661 nm. The maximum fluorescence emission wavelength is 667 nm. Furthermore, the simulated S-band absorption of chlorin compounds (compounds 1–3) has a maximum wavelength of about 361 nm, and the Q band absorption is up to 600 nm, with f_{\max} values ranging between 0.2139 and 0.2242. By comparison, the calculated S band of chlorophyll *a* compounds (compounds 4–9) with an external five-

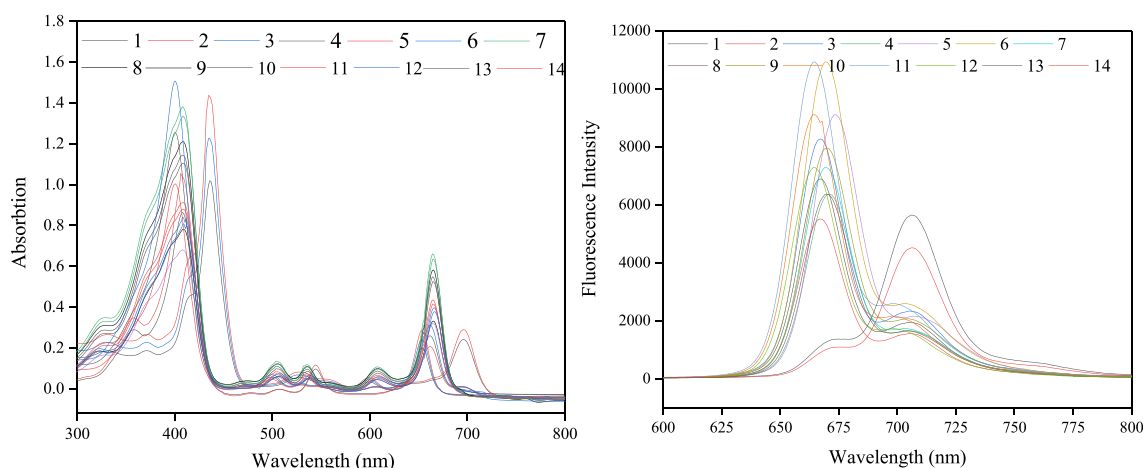


Fig. 5. Absorption and fluorescence spectrum of Chls in methanol.

membered ring structure has a red shift of 8 to 9 nm, and the Q band has a red shift of 5 to 6 nm. The simulated spectra of chlorophyll *a* compounds and chlorin compounds are very similar. The red shift in the absorption wavelength of chlorophyll *a* compounds might be caused by the *trans*-ring effect of the external five-membered ring. That is, the chromophores (carbonyl group) in the five-membered ring system is conducive to the interaction between the electron orbitals, enhancing the wavelength of the absorption band as well as the absorption. Additionally, the f_{\max} of chlorophyll *a* compounds ranges from 0.2357 to 0.2636, indicating that their absorption intensity for near-infrared light is stronger than those of chlorin compounds.

Compared with the chlorin compounds, the chlorophyll *b* compounds (compounds 10–12) have a red shift of 34 to 36 nm in the S band, and a blue shift of 6 nm in the Q band. Meanwhile, the simulated spectral data show a red shift of approximately 22 nm in the S band and a blue shift of 25 ~ 28 nm in the Q band. Furthermore, the f_{\max} values of chlorophyll *b* compounds range from 0.1381 to 0.1490, indicating weaker absorption intensity for near-infrared light than other Chls. The oxygen atoms of the aldehyde group of chlorophyll *b* compounds exist in the form of sp^2 hybridization, which increases the conjugated system of the molecule in the x-axis direction and causes the S band to red shift. The electron-withdrawing effect of the aldehyde group drives the four orbitals of HOMO, HOMO + 1, HOMO and HOMO-1 toward lower energy levels. In detail, the b_2 orbital is most heavily affected, while the c_1 orbital is least influenced, resulting in a larger energy gap between b_2 and c_2 , thus leading to a blue shift in the absorption band at Q. Due to the blue shift of the maximum absorption wavelength of chlorophyll *b* compounds and the weaker absorption intensity in the Q region than other Chls, it is not conducive to the capture of near-infrared energy. Therefore, chlorophyll *b* compounds are not good photosensitizer candidates.

Compared with chlorin compounds, purpurin 18a compounds demonstrate a red shift of approximately 6 nm in the S band and a larger red shift of about 40 nm in the Q band. In addition, the six-membered ring greatly influences the b_2 and c_1 orbitals, producing a smaller energy gap between b_2 and c_2 and a red shift of the Q band. Additionally, the f_{\max} values of purpurin 18 compounds range from 0.2825 to 0.3032, indicating a stronger absorption intensity for near-infrared light than other Chls. In this case, the excitation light of purpurin 18a compounds possesses stronger penetration abilities into tissue cells and a heightened capability to capture near-infrared energy. Therefore, purpurin 18a compounds could serve as promising candidates for PSs.

The rigid plane in the molecular structure can largely affect the fluorescence intensity of the photosensitizer. There are delocalized π bond in the Chls, and its fluorescence is mainly generated by the $\pi \rightarrow \pi^*$ radiative transition emission. By comparing the absorption spectra and emission spectra, it is clear that they show a certain mirror symmetry relationship (Fig. 5). The emission spectra of Chls have different degrees of red shift relative to the absorption spectra. This can be attributed to the vertical transition of the ground state to the corresponding first excited singlet state, and its stable configuration changes (Deng et al., 2023, Li et al., 2023, Pandey et al., 2023). The electrons transition from HOMO to LUMO, and the bonding mode changes.

3.6. Photostability

An ideal PSs should possess good photostability under light conditions to ensure the continuous production of ROS. Typically, the photo-induced degradation by PSs is accompanied by structural breakage, resulting in degradation products without exhibiting characteristic absorption of the porphine nucleus, commonly referred to as bleaching (Rizzi et al., 2021). In this study, we assessed the degree of photobleaching using the change of PSs absorption intensity (I_t/I_0) after illumination. As depicted in Fig. 6, after 10 min illumination, the 14 tested Chls have retention rates above 80 %. Among them, chlorophyll *b* compounds (compounds 10–12) exhibit the best stability, with a

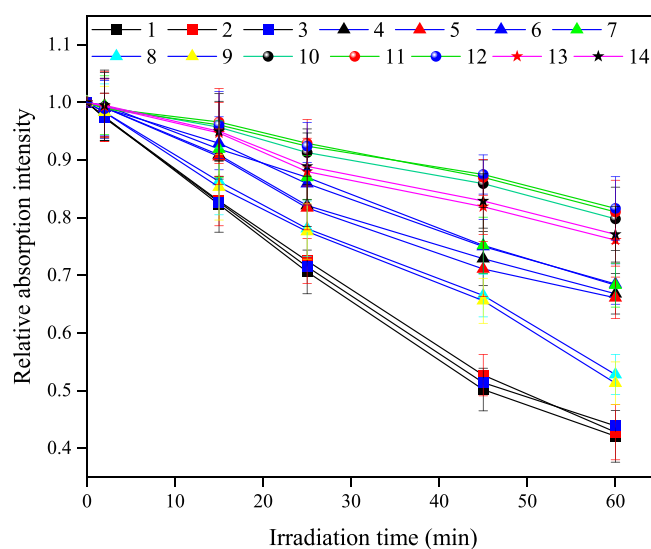


Fig. 6. Degradation rate of 14 Chls under 660 nm light irradiation.

retention rate still exceeding 80 % after 60 min irradiation. Followed by the purpurin compounds (compounds 13 and 14), they still retained more than 76.5 % after 60 min irradiation. By contrast, chlorin compounds (compounds 1–3) demonstrate the poorest photostability, with a retention rate of less than 34.5 % after 60 min. Furthermore, it was observed that methylated chlorin e6 dimethyl ester and chlorin e6 trimethyl ester exhibited better photostability compared to unmethylated chlorin e6. In addition, Chls containing phytol long chains demonstrate better photostability than corresponding saponified Chls without phytol long chains. Our findings indicate that the esterification of methyl or phytol long chains on carboxyl groups R2, R5, and R6 of chlorophyll porphins can significantly enhance the photostability of Chls since the esterification process greatly decreases the total electron energy of Chls. Conversely, the stability is reduced if R2, R5, and R6 are carboxyl groups.

3.7. In vitro ROS assay for chlorophyll derivatives

3.7.1. The ability of Chls to produce ROS

During the experiment, DPBF was used as ROS capture agent, and methylene blue (MB, ROS yields $\Phi(^1O_2) = 0.49$) was used as a reference to determine the ROS yields of 14 Chls. The experimental results indicated that chlorin compounds (compounds 1–3) exhibit the highest ROS yields, followed by chlorophyll *a* compounds (compounds 4–9), purpurin 18 compounds (compounds 13 and 14). Chlorophyll *b* compounds (compounds 10–12) have the lowest ROS yields (Fig. 7). Fig. S22 provided additional insights into the factors controlling ROS production. The electronegativity of the studied compounds follows the sequence of chlorin compounds > chlorophyll *a* compounds > purpurin 18 compounds > chlorophyll *b* compounds. The results indicate that the peripheral substituents of the porphin parent ring affect the electron density of the porphin macrocycle of Chls, and the electronegativity of the porphin macrocycle of Chls is positively correlated with the ROS yields. In this scenario, we can infer that the electronegativity of the chlorophyll compound porphine macrocycle promotes the energy transfer between the photosensitizer and the molecular oxygen during the type II photoreaction of the green compound photosensitizer (Cao et al., 2017). Furthermore, purpurin compounds exhibit significantly higher absorption coefficients in the Q band compared to other Chls. Studies have shown that the absorption coefficient at the maximum absorption wavelength in the Q band also has an impact on the ROS yields. The greater the absorption coefficient, the higher the ROS yields (Hao, 2022, Guo, 2021, Hu, 2022). Additionally, the external six-

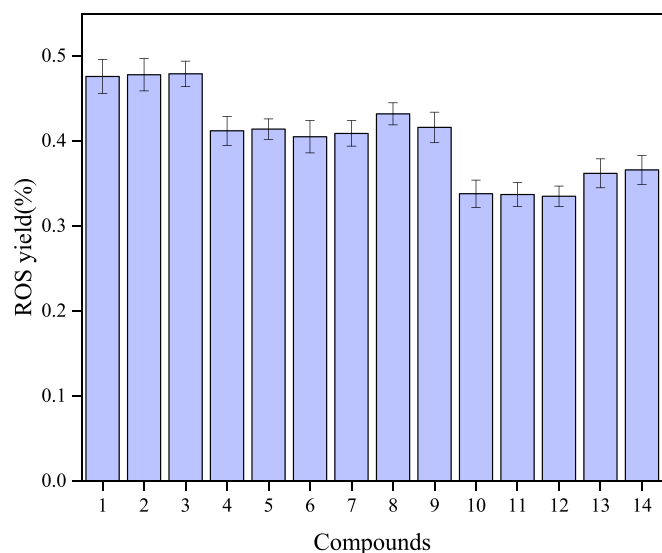


Fig. 7. 14 ROS yield of Chls in DMF.

membered ring of purpurin increases the conjugation of porphine macrocycle and thus decreases the E_g , resulting in good chemical reactivity and polarizability of purpurin compounds and ultimately improving their ROS production ability. Consequently, purpurin 18 compounds exhibit higher ROS yields compared to chlorophyll *b* compounds. Chls with phytyl (compounds 4, 8 and 14) have ROS yields similar to their saponified counterparts (compounds 5, 9 and 13). Similarly, chlorin e6 and chlorin methyl ester compounds (compounds 2 and 3) have identical ROS yields. These results suggest that the methyl esterification and phytoesterification of the carboxyl groups (R1, R5, R6) around the porphin macrocycle of Chls has a little effect on the ROS yields of Chls in solvents.

3.7.2. Intracellular ROS production of Chls

The results of intracellular ROS production of 14 Chls differ from those in DMF *in vitro*. The results in DMF *in vitro* show that the ROS yields of Chls with the phytyl group (compounds 4, 8 and 14) are basically consistent with those of the saponified ones without phytyl group (compounds 5, 9 and 13). However, the intracellular ROS production rates of Chls with phytyl (compounds 4, 8 and 14) are significantly lower than those of Chls without phytyl (compounds 5, 9 and 13) (Figs. 8 and

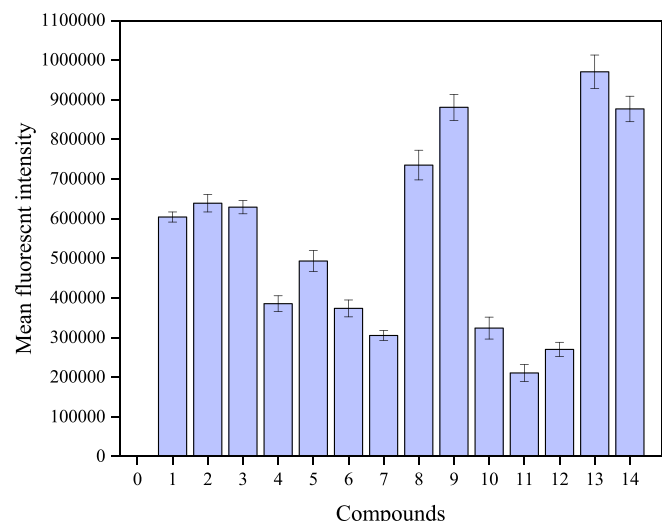


Fig. 8. Qualitative analysis of mean fluorescence intensity in 4 T1 cells.

9). This is likely because the presence of the long-chain phytyl persad hinder the entry of the compound into the cell, as its size could be too large for efficient cellular uptake. In addition, the long chain of phytyl will also reduce the solubility of GBChls. According to Table 4, the logP of GBChls (compounds 5, 9 and 13) without phytyl long chain is between 1 and 3, and the solubility is good. It is easy to enter the cell through passive diffusion, while the logP of GBChls (compounds 4, 6, 7, 8, 10, 11, 12 and 14) containing phytyl long chain is greater than 5, with poor solubility, difficult to be absorbed, and poor bioavailability.

13^2-OH pheophytin a and a' (compounds 6 and 7) have similar ROS yields in DMF, as well as the yields of pheophytin b and b' (compounds 11 and 12). However, the intracellular ROS production rate of 13^2-OH pheophytin a' and b' (compounds 7 and 12) is significantly lower than that of 13^2-OH pheophytin a and b (compounds 6 and 11). As shown in Fig. S22, 13^2-OH pheophytin a' and b' exhibits an L-shape configuration, where the porphin macrocycle is perpendicular to the plane where the phytyl group is located. In contrast, the porphin macrocycle of 13^2-OH pheophytin a and b is inclined at about 60 degrees from the plane where the phytyl group is situated, which is significantly less than 90 degrees. Based on these observations, we can infer that the larger spatial volume of 13^2-OH pheophytin a' and b' may hinder their entry into cell membranes and organelles. Consequently, this less efficient accessibility could lead to a lower intracellular ROS production rate.

Chlorin compounds (compounds 1–3) exhibit the highest ROS yields in DMF. However, the intracellular ROS productions of pyro-pheophytin compounds (compounds 8 and 9) and purpurin compounds (compounds 13 and 14) are higher than those of chlorin compounds. This difference may be attributed to the spatial structure of the molecules. In pyro-pheophytin compounds (compounds 8 and 9), the E ring and porphyrin macrocycle are coplanar, and there are no additional groups at position 13^2 . Furthermore, in pyro-pheophytin a and phy-purpurin 18a, the phytyl long chain at position 17^3 is folded together with the porphyrin macrocycle, resulting in a flat overall molecular structure. This conformation is preferential for the molecule to enter the cell membrane during the process of molecular transport, thus increasing in intracellular ROS yields. Contrarily, chlorin chlorophyll does not have corresponding E-ring binding at positions 13 and 15. Furthermore, the groups and porphin macrocycle at 13 and 15 are L-shaped in spatial structure, in which the parent ring structure is perpendicular to the plane where the side chain is located. This conformation hampers the entry of molecules into the cell membrane and organelles, thereby the intracellular ROS production is reduced.

4. Conclusions

GBE illustrates the great potential of its application in treating various diseases (e.g., hypertension, senile dementia and tumors). GBE and GBPPs processing will generate a large amount of chlorophyll-rich wastes, in which some chlorophylls show excellent pharmacological functions. In this study, we prepared 14 GBChls from GBL and GBE processing wastes. We further evaluate the physical and chemical properties of the 14 GBChls using experiments and theoretical simulation. Our results highlight two PPs (purpurin 18 and chlorin e6) display superior performance as photosensitizers (PSs) in photodynamics therapy.

The esterification of GBChls, especially the esterification of the phytol, can increase the photostability of GBChls and simultaneously reduce the uptake rate and bioavailability of cells, thus decreasing intracellular ROS production. The electron absorption effect of GBChls at R_2 (aldehyde group) can increase E_g , weaken Q band absorption and facilitate the blue shift. However, the electron-giving (methyl) effect at R_2 and the conjugation effect of the E ring (six-membered ring) of GBChls can effectively reduce E_g , enhance Q-band absorption and facilitate redshift. In particular, the electron-giving effect of porphyrin rings can promote the energy transfer from PPs to molecular oxygen in the type II photoreaction of chlorophyll photosensitizer. The mechanism

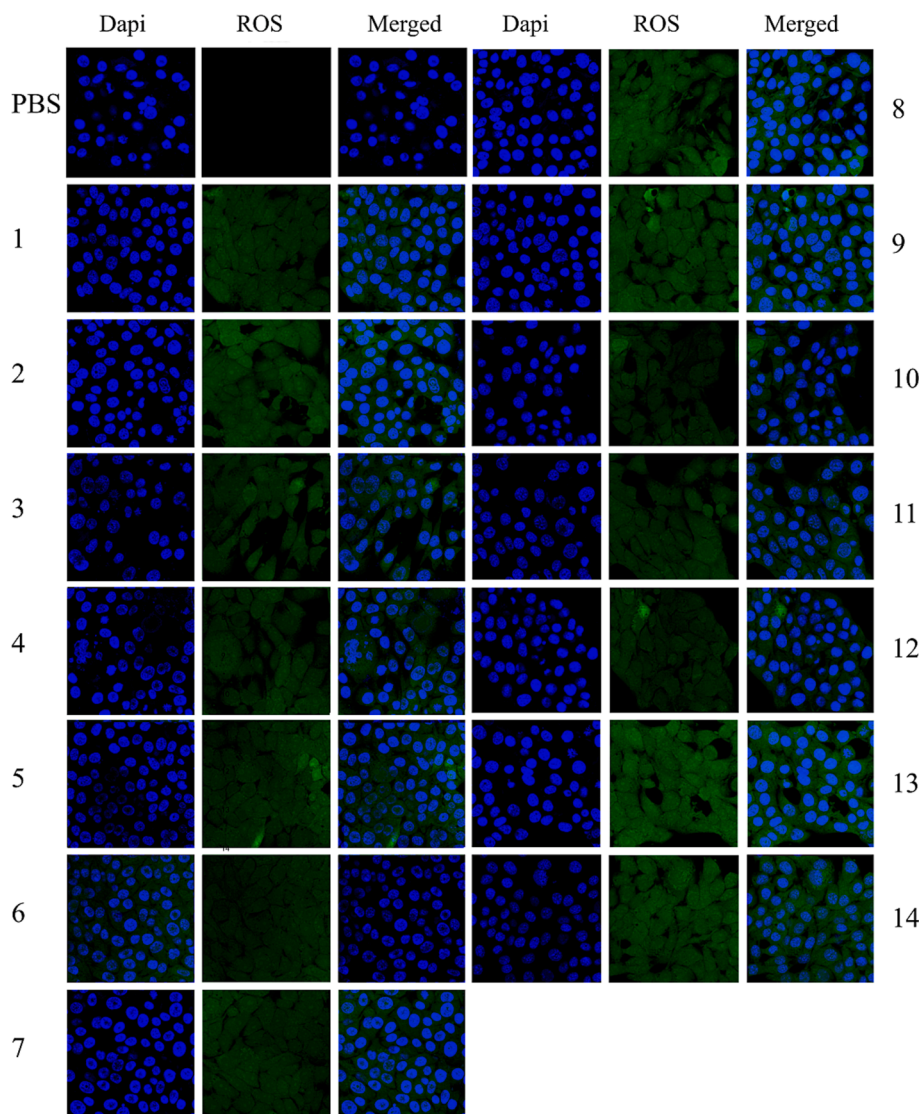


Fig. 9. The ROS production of Chls observed by CLSM.

Table 4

The logP parameters of 14 Chls were calculated using ChemDrawr software.

| Compounds | 1 | 2 | 3 | 4 | 5 | 6 | 7 | 8 | 9 | 10 | 11 | 12 | 13 | 14 |
|-----------|------|------|------|------|------|------|------|-------|------|------|------|------|------|-------|
| logP | 2.23 | 3.17 | 2.85 | 9.69 | 2.19 | 9.45 | 9.45 | 10.04 | 2.53 | 9.19 | 8.94 | 8.94 | 2.73 | 10.23 |

logP: oil - water partition coefficient.

of GBChls in PDT is that GBChls combine with oxygen in target cells to produce cytotoxic ROS under the action of excitation light. PPs produce ROS mainly through type I and type II photoreactions. It has yet to be clearly explored which pathway of GBChls mainly produces ROS and the influence of various groups on type I and type II photoreactions. Therefore, further optimization and research are required to provide the basis for drug development.

Declaration of competing interest

The authors declare that they have no known competing financial interests or personal relationships that could have appeared to influence the work reported in this paper.

Acknowledgments

This work was supported by State Project of Key Research & Development of Science and Technology (2022YFD2200605); and National Natural Science Foundation of China (32101473).

Appendix A. Supplementary material

Supplementary data to this article can be found online at <https://doi.org/10.1016/j.arabjc.2023.105549>.

References

- Arnaut, L.G., Pereira, M.M., 2023. Overcoming the challenges of infrared photosensitizers in photodynamic therapy: The making of redaporfin. *Chem. Commun.* 59, 9457–9468. <https://doi.org/10.1039/D3CC02283H>.

- Bartusik-Aebisher, D., Woźnicki, P., Dynarowicz, K., et al., 2023. Photosensitizers for photodynamic therapy of brain cancers—A review. *Brain Sci.* 13, 1299. <https://doi.org/10.3390/brainsci13091299>.
- Boateng, I.D., 2023. Ginkgols and bilobols in Ginkgo biloba L. A review of their extraction and bioactivities. *Phytother. Res.* <https://doi.org/10.1002/ptr.7877>.
- Bourne-Worster, S., Feighan, O., Manby, F.R., 2023. Charge transfer as a mechanism for chlorophyll fluorescence concentration quenching. *Proc. Natl. Acad. Sci.* 120, e2210811120 <https://doi.org/10.1073/pnas.2210811120>.
- Brandis, A. S., Salomon, Y., Scherz, A., 2006. Chlorophyll sensitizers in photodynamic therapy[M]//Chlorophylls and bacteriochlorophylls: biochemistry, biophysics, functions and applications. Dordrecht: Springer Netherlands, 2006, 461-483. https://doi.org/10.1007/1-4020-4516-6_32.
- Cai, J.Q., Liu, X.M., Gao, Z.J., et al., 2021. Chlorophylls derivatives: Photophysical properties, assemblies, nanostructures and biomedical applications. *Mater. Today* 45, 77–92. <https://doi.org/10.1016/j.mattod.2020.11.001>.
- Cao, L., Guo, X., Wang, L., Wang, S., Li, Y., Zhao, W., 2017. Synthesis and *in vitro* phototoxicity of novel π -extension derivatives of chlorin e6. *New J. Chem.* 41, 14279–14287. <https://doi.org/10.1039/c7nj03279j>.
- Chen, K., Roca, M., 2018. Cooking effects on chlorophyll profile of the main edible seaweeds. *Food Chem.* 266, 368–374. <https://doi.org/10.1016/j.foodchem.2018.06.040>.
- Chen, W., Zheng, Y., Wang, J., et al., 2023. Ethylene-responsive SbWRKY50 suppresses leaf senescence by inhibition of chlorophyll degradation in sorghum. *New Phytol.* 238, 1129–1145. <https://doi.org/10.1111/nph.18757>.
- Chin, J.D., Zhao, L., Mayberry, T.G., et al., 2023. Photodynamic therapy, probiotics, acetic acid, and essential oil in the treatment of chronic wounds infected with *Pseudomonas aeruginosa*. *Pharm.* 15, 1721. <https://doi.org/10.3390/pharmaceutics15061721>.
- Choudhury, A.K., Sarkar, R., Bhuyan, J., 2023. Histamine-bound magnesium porphyrins: diverse coordination modes, inhibitory role in photodegradation of chlorophyll a and antioxidant activity. *Dalton Trans.* 52, 11085–11095. <https://doi.org/10.1039/D1CP01943K>.
- Deng, C., Zheng, M., Han, S., et al., 2023. GSH-activated porphyrin sonosensitizer prodrug for fluorescence imaging-guided cancer sonodynamic therapy. *Adv. Funct. Mater.*, 2300348 <https://doi.org/10.1002/adfm.202300348>.
- Diers, J.R., Kirmaier, C., Taniguchi, M., et al., 2021. A perspective on the redox properties of tetrapyrrole macrocycles. *Phys. Chem. Chem. Phys.* 23, 19130–19140. <https://doi.org/10.1039/D3DT01309J>.
- Duan, Hq, Takaishi, Y, Momama, H; et al, 2002. Immunosuppressive constituents from *Saussurea medusa*. *Phytochemistry.* 59, 85–90. [https://doi.org/10.1016/S0031-9422\(01\)00429-0](https://doi.org/10.1016/S0031-9422(01)00429-0).
- Duan, S., Sasaki, S., Han, D., et al., 2023. Natural bio-additive chlorophyll derivative enables 17.30% efficiency organic solar cells. *Adv. Funct. Mater.*, 2302820 <https://doi.org/10.1039/D3DT01309J>.
- Guo, J., Feng, K., Wu, W., et al., 2021. Smart 131I-labeled self-illuminating photosensitizers for deep tumor therapy. *Angew. Chem. Int. Ed.* 60, 21884–21889. <https://doi.org/10.1002/anie.202107231>.
- Hao, B., Wang, J., Wang, C., et al., 2022. Bridging D-A type photosensitizers with the azo group to boost intersystem crossing for efficient photodynamic therapy. *Chem. Sci.* 13, 4139–4149. <https://doi.org/10.1039/D2SC00381C>.
- Hooper, J.K., Sery, T.W., Yamamoto, N., 2010. Photodynamic sensitizers from chlorophyll:purpurin-18 and chlorin6. *Photochem. Photobiol.* 48, 579–582. <https://doi.org/10.1111/j.1751-1097.1988.tb02867.x>.
- Hu, X., Gu, T., Khan, I., et al., 2021. Research progress in the interconversion, turnover and degradation of chlorophyll. *Cells* 10, 3134. <https://doi.org/10.3390/cells10113134>.
- Hu, L.Q., Xu, D.Y., 2010. HPLC separation and characterization of chlorin derivatives with intact ring V from acid degradation products of silkworm excrement crude chlorophyll mixture. *Biomed. Chromatogr.* 3, 72–74. <https://doi.org/10.1002/bmc.1130030207>.
- Hu, X., Zhang, H., Wang, Y., et al., 2022. Synergistic antibacterial strategy based on photodynamic therapy: Progress and perspectives. *Chem. Eng. J.* 450, 138129 <https://doi.org/10.1016/j.cej.2022.138129>.
- Jiang, D., Li, H., Wang, S., et al., 2023. Insight the CO₂ adsorption onto biomass-pyrolysis derived char via experimental analysis coupled with DFT calculation. *Fuel* 332, 125948. <https://doi.org/10.1016/j.fuel.2022.125948>.
- Kang, Y.R., Park, J., Jung, S.K., et al., 2018. Synthesis, characterization, and functional properties of chlorophylls, pheophytins, and Zn-pheophytins. *Food Chem.* 245, 943–950. <https://doi.org/10.1016/j.foodchem.2017.11.079>.
- Kang, S.H., Zhou, H., Kim, H.K., 2023. D- π A structured porphyrin sensitizers for dye-sensitized solar cells. *J. Porphyrins Phthalocyanines* 27, 226–232. <https://doi.org/10.1142/S1088424622500821>.
- Lan, M., Zhao, S., Liu, W., et al., 2019. Photosensitizers for photodynamic therapy. *Adv. Healthc. Mater.* 8, 1900132 <https://doi.org/10.1002/adhm.201900132>.
- Leal, J., Durá, G., Jalón, F.A., et al., 2023. Luminescent cyclometalated platinum compounds with N, P, and O ligands: Density-functional theory studies and analysis of the anticancer potential. *Appl. Organomet. Chem.* 37, e6983. <https://doi.org/10.1002/aoc.6983>.
- Li, F., Boateng, I.D., Yang, X.M., et al., 2023. Effects of processing methods on quality, antioxidant capacity, and cytotoxicity of Ginkgo biloba leaf tea product. *J. Sci. Food Agric.* 103, 4993–5003. <https://doi.org/10.1002/jsfa.12577>.
- Li, M., Zhang, S., Li, H., et al., 2023. Cerium/polyacrylic acid modified porphyrin metal-organic framework as fluorescence and photothermal sensor for ascorbic acid measurement. *Talanta* 252, 123825. <https://doi.org/10.1016/j.talanta.2022.123825>.
- Liao, S., Cai, M., Zhu, R., et al., 2023. Antitumor effect of photodynamic therapy/sonodynamic therapy/sono-photodynamic therapy of chlorin e6 and other applications. *Mol. Pharma.* 20, 875–885. <https://doi.org/10.1021/acs.molpharmaceut.2c00824>.
- Liu, X.G., Lu, X., Gao, W., et al., 2022. Structure, synthesis, biosynthesis, and activity of the characteristic compounds from *Ginkgo biloba* L. *Nat. Prod. Rep.* 39, 474–511. <https://doi.org/10.1039/D1NP00026H>.
- Liu, Y.T., Luo, L.L., Zhu, H., et al., 2021. En route to the transformation of porphyrin molecules for PDT: Theoretical insights on the reactive oxygen generation of 1D nano-wires and 2D covalent organic frameworks[J]. *Chem. Phys.* 2021 (549), 111278 <https://doi.org/10.1016/j.chemphys.2021.111278>.
- Lu, H., Zada, S., Tang, S., et al., 2022. Artificial photoactive chlorophyll conjugated vanadium carbide nanostructure for synergistic photothermal/photodynamic therapy of cancer. *J. Nanobiotechnol.* 20 (1), 121. <https://doi.org/10.1186/s12951-022-01331-x>.
- Pandey, V., Janaagal, A., Jain, A., et al., 2023. A2B2 type porphyrins with meso-donor groups: Synthesis, X-ray structures, DFT studies and photocatalytic application using sunlight. *Dyes Pigm.* 209, 110861 <https://doi.org/10.1016/j.dyepig.2022.110861>.
- Pérez-Gálvez, A., Roca, M., 2023. Comprehensive chlorophyll composition of commercial green food colorants and coloring foodstuffs by HPLC-ESI-QTOF-MS/MS: Chlorophyllins. *Food Chem.* 415, 135746 <https://doi.org/10.1016/j.foodchem.2023.135746>.
- Pucci, C., Martinielli, C., Degl'Innocenti, A., et al., 2021. Light-activated biomedical applications of chlorophyll derivatives. *Macromol. Biosci.* 21, 2100181. <https://doi.org/10.1002/mabi.202100181>.
- Qiu, Y., Guo, X., Zhang, C., et al., 2023. Dual-photosensitizer nanopatform based on near-infrared excitation orthogonal emission nanomaterials for enhanced photodynamic therapy of tumors. *ACS Appl. Bio Mater.* <https://doi.org/10.1021/acscabm.3c00212>.
- Reiter, S., Bäuml, L., Hauer, J., et al., 2022. Q-Band relaxation in chlorophyll: new insights from multireference quantum dynamics. *Phys. Chem. Chem. Phys.* 24, 27212–27223. <https://doi.org/10.1039/D2CP02914F>.
- Rizzi, V., Gubitosa, J., Fini, P., et al., 2021. Development of *Spirulina* sea-weed raw extract/polyamidoamine hydrogel system as novel platform in photodynamic therapy: Photostability and photoactivity of chlorophyll a. *Mater. Sci. Eng.* 119, 111593 <https://doi.org/10.1016/j.msec.2020.111593>.
- Da Rocha, V. N., Köhler, M. H., Nagata, K., et al., 2023. Theoretical study of C6F5-corrole molecules functionalized with aromatic groups for Photodynamic Therapy. *Spectrochim. Acta, Part A.* 293, 122500. <https://doi.org/10.1016/j.saa.2023.122500>.
- Sammüller, F., Hermann, S., Schmidt, M., 2023. Comparative study of force-based classical density functional theory. *Phys. Rev. E* 107, 034109. <https://doi.org/10.1103/PhysRevE.107.034109>.
- Shen, H., Zhang, C. wei., Chen, H. xia., et al., 2023. Extraction, isolation and structural identification of pigments from *Ginkgo biloba* leaves. *Forest Chem Industry.* 43, 79–88. <http://qikan.cqvip.com/Qikan/Article/Detail?id=7108997996>.
- Singh, S.K., Mazumder, S., Vincy, A., et al., 2023. Review of photoresponsive plasmonic nanoparticles that produce reactive chemical species for photodynamic therapy of cancer and bacterial infections. *ACS Appl. Nano Mater.* 6, 1508–1521. <https://doi.org/10.1021/acsnanm.2c04551>.
- Szafraniec, M.J., 2023. Interactions of chlorophyll-derived photosensitizers with human serum albumin are determined by the central metal ion. *J. Biomol. Struct. Dyn.* 41, 479–492. <https://doi.org/10.1080/07391102.2021.2007794>.
- Udrea, A.M., Smarandache, A., Dinache, A., et al., 2023. Photosensitizers-loaded nanocarriers for enhancement of photodynamic therapy in melanoma treatment. *Pharm.* 15, 2124. <https://doi.org/10.3390/pharmaceutics15082124>.
- Wahnou, H., Youlyouz-Marfaq, I., Liagre, B., et al., 2023. Shining a light on prostate cancer: Photodynamic therapy and combination approaches. *Pharm.* 15, 1767. <https://doi.org/10.3390/pharmaceutics15061767>.
- Wang, J., Gong, Q., Jiao, L., et al., 2023. Research advances in BODIPY-assembled supramolecular photosensitizers for photodynamic therapy. *Coord. Chem. Rev.* 496, 215367 <https://doi.org/10.1016/j.ccr.2023.215367>.
- Wang, P., Grimm, B., 2021. Connecting chlorophyll metabolism with accumulation of the photosynthetic apparatus. *Trends Plant.* 26, 484–495. <https://doi.org/10.1016/j.tplants.2020.12.005>.
- Wang, H.T., Ou, L.Y., Chen, T.A., et al., 2023. Refrigeration, forchlorfenuron, and gibberellic acid treatments differentially regulate chlorophyll catabolic pathway to delay yellowing of broccoli. *Postharvest Biol. Technol.* 197, 112221 <https://doi.org/10.1016/j.postharvbio.2022.112221>.
- Warszyńska, M., Repetowski, P., Dąbrowski, J.M., 2023. Photodynamic therapy combined with immunotherapy: Recent advances and future research directions. *Coord. Chem. Rev.* 495, 215350 <https://doi.org/10.1016/j.ccr.2023.215350>.
- Yang, L., Wang, C., Ye, J., et al., 2011. Hepatoprotective effects of polyphenols from *Ginkgo biloba* L. leaves on CCl₄-induced hepatotoxicity in rats. *Fitoterapia* 82, 834–840. <https://doi.org/10.1016/j.fitote.2011.04.009>.
- Zahra, M., Chota, A., Abrahamse, H., et al., 2023. Efficacy of green synthesized nanoparticles in photodynamic therapy: A therapeutic approach. *Int. J. Mol. Sci.* 24, 10931. <https://doi.org/10.3390/ijms241310931>.
- Zhang, A., Kwan, L., Stillman, M.J., 2017. The spectroscopic impact of interactions with the four Gouterman orbitals from peripheral decoration of porphyrins with simple electron withdrawing and donating groups. *Org. Biomol. Chem.* 15, 9081–9094. <https://doi.org/10.1039/C7OB01960B>.

Zhang, S., Yang, W., Lu, X., et al., 2023. Near-infrared AIEgens with high singlet-oxygen yields for mitochondria-specific imaging and antitumor photodynamic therapy. *ACS Chem. Neurosci.* 14, 7076–7085. <https://doi.org/10.1039/D3SC00588G>.

Zheng, X., Lei, S.N., Gao, Z., et al., 2023. Supramolecular photosensitizers using extended macrocyclic hosts for photodynamic therapy with distinct cellular delivery. *Chem. Sci.* 14, 3523–3530. <https://doi.org/10.1039/D3SC00107E>.

Zhou, W., Jiang, X., Zhen, X., 2023. Development of organic photosensitizers for antimicrobial photodynamic therapy. *Biomater. Sci.* <https://doi.org/10.1039/D3BM00730H>.